



OPEN

Surveying soil-borne disease development on wild rocket salad crop by proximal sensing based on high-resolution hyperspectral features

Angelica Galieni¹, Nicola Nicastro², Alfonso Pentangelo², Cristiano Platani¹, Teodoro Cardi^{2,3} & Catello Pane²✉

Wild rocket (*Diplotaxis tenuifolia*, Brassicaceae) is a baby-leaf vegetable crop of high economic interest, used in ready-to-eat minimally processed salads, with an appreciated taste and nutraceutical features. Disease management is key to achieving the sustainability of the entire production chain in intensive systems, where synthetic fungicides are limited or not permitted. In this context, soil-borne pathologies, much feared by growers, are becoming a real emergency. Digital screening of green beds can be implemented in order to optimize the use of sustainable means. The current study used a high-resolution hyperspectral array (spectroscopy at 350–2500 nm) to attempt to follow the progression of symptoms of Rhizoctonia, Sclerotinia, and Sclerotium disease across four different severity levels. A Random Forest machine learning model reduced dimensions of the training big dataset allowing to compute de novo vegetation indices specifically informative about canopy decay caused by all basal pathogenic attacks. Their transferability was also tested on the canopy dataset, which was useful for assessing the health status of wild rocket plants. Indeed, the progression of symptoms associated with soil-borne pathogens is closely related to the reduction of leaf absorbance of the canopy in certain ranges of visible and shortwave infrared spectral regions sensitive to reduction of chlorophyll and other pigments as well as to modifications of water content and turgor.

Wild rocket (*Diplotaxis tenuifolia* [L.] D.C.) is a leafy vegetable crop belonging to the *Brassicaceae* family, cultivated in many temperate areas worldwide for fresh consumption in salad preparations, and appreciated for the characteristic pungency, intense peppery flavour, antioxidant activity and other health-promoting phytonutrients^{1–3}. This baby-leaf crop has a significant economic interest particularly with reference to the specific high-convenience food chain⁴. Nowadays, Italy is the major European producing country of packaged wild rocket, cultivated on around 6000 ha under unheated plastic greenhouses^{5,6}. Because of intensive farming, multiple harvesting cycles *per* sowing season at 20–40 days intervals⁷, specific protocols, based on low-impacting agrotechniques, are necessary with the crucial aim to avoid pesticide residues in the product and obtain premium quality fresh-cuttings associated with improved aesthetic look, taste, nutraceutical properties and shelf-life potential^{8–10}. Nevertheless, the growing conditions, general cultivar susceptibility to pathogens and the requested lower use of fungicides make the crop prone to recrudescence and/or re-emergence of soil-borne pathologies^{11–13}, such as *Rhizoctonia solani* Kühn and *Sclerotinia sclerotiorum* (Lib.) de Bary, which can cause devastating lawn rotting and yield losses impacting the farmer economy in the short and mid-term^{11,14,15}. These soil-borne pathologies rise to a real emergency in the intensive biological management systems and anywhere synthetic fungicides are banned or not permitted^{16–20}. Valuable alternatives applicable in the management programs, need to be further improved in terms of use efficiency²¹. Digital technologies that analyse the light reflected from crop foliage in a wide wavelength range of the electromagnetic spectrum can aid in the making decision process aiming to crop

¹Council for Agricultural Research and Economics (CREA), Research Centre for Vegetable and Ornamental Crops, via Salaria 1, 63077 Monsampolo del Tronto, Italy. ²Council for Agricultural Research and Economics (CREA), Research Centre for Vegetable and Ornamental Crops, via Cavaleggeri 25, 84098 Pontecagnano Faiano, Italy. ³Present address: CNR-IBBR, Institute of Biosciences and BioResources, via Università 133, 80055 Portici, Italy. ✉email: catello.pane@crea.gov.it

protection targeted strategies based on a reduced use of pesticides^{22,23}. For example, Manganiello et al.²⁴ recently selected high-performing hyperspectral vegetative indices (VIs), such as Soil Adjusted Vegetation Index (SAVI) group and Triangular Vegetation Index (TVI), able to track *Trichoderma* spp. biocontrol strains in counteracting multiple soil borne diseases of baby leaf vegetables, including *R. solani* on wild rocket, opening the way to precision biological control applications.

The non-imaging technology is based on the application of high-resolved reflectance spectroscopy to acquire the punctual spectral fingerprints of a plant at foliar and/or canopy level, interrelated to its chemical-physical attributes, in order to provide useful remote sensed information on the plant status. Previous studies demonstrated the accuracy of hyperspectral optical sensing to well classified plant diseases and configure reference outlines for the proximal surveying of crop healthiness²⁵. Karadağ et al.²⁶ improved a method based on 350–2500 nm spectral reflectance for the *Fusarium* disease severity estimation on pepper. On peanut, reflectance data have been used to identify the disease stage of the bacterial wilting caused by *Ralstonia solanacearum*²⁷. Junges et al.²⁸ applied hyperspectral scouting to discriminate the described symptomatology associated with the grapevine decline and death syndrome. In tomato, following a laboratory-to-field approach, Abdulridha et al.²⁹ pointed up hyperspectral surveying cultivations affected by non-specific leaf spotting at different stages, caused by the fungus *Corynespora cassicola* and the bacterium *Xanthomonas perforans*.

The above-mentioned technologies offer new opportunities to devise innovative tools for supporting the sustainable soil-borne disease management of leafy vegetables, increasing the farmers' monitoring capability to early identify outbreaks and apply a timely and spatially effective phytosanitary intervention, especially under continuous sequences in Mediterranean-type climate regions³⁰. However, a basic computational study to filter the acquiring big data into more manageable synthetic hyperspectral indices is a decisive step to make the proposed digital tool exploitable in practical applications on crops with acceptable costs³¹. Therefore, this study aimed at the evaluation of the disease-specific hyperspectral signatures of wild rocket plants artificially inoculated, under laboratory conditions, with three soil-borne pathogens (*R. solani*, *S. sclerotiorum* and *Sclerotium rolfsii* Sacc.). To this purpose, wild rocket plants were subjected to hyperspectral data acquisition using a non-imaging hyperspectral sensor. The first objective was to obtain a high-resolution assessment of the differences among spectral signatures of healthy and infected (at different disease levels) plants at leaf scale, and thus the selection of the most discriminant wavelengths. This information was used to set specific de novo synthetic VIs under the most stable environmental conditions, without risk of changing environmental factors (i.e., using the sensor as an active sensor), through a Machine Learning pipeline using the Random Forest (RF) algorithm. The second objective was to understand factors affecting the use of newly developed VIs at plant/canopy scale (i.e., at pot scale and using the sensor as passive sensor), assessing their transferability to high-throughput experiments for practical applications. The methodology devised in the present study can be of larger applicability in other crop—(soil-borne) pathogen systems.

Materials and methods

The present study was conceptualized and conducted based on two independent experiments, named “guide experiment” (Exp_Gui) and “applicative experiment” (Exp_App), following the workflow shown in Fig. S1.

Leaf and canopy reflectance data (see the “[Reflectance measurements](#)” section) were collected from soil-inoculated wild rocket plants grown in controlled environments. From Exp_Gui we obtained leaf-scale reflectance data. The resulting dataset was used for calibration and validation purposes, and then divided into a “training dataset” and a “testing dataset” (see the “[Data preparation and analysis](#)” section), to model spectral responses at increasing levels of disease severity, and to develop new VIs capable of monitoring aerial symptoms of soil-borne diseases in wild rocket. Reflectance data at canopy scale were acquired from Exp_App. The resulting dataset, called the “canopy dataset”, was used to evaluate the applicability of the newly developed VIs using plant growth and data acquisition conditions comparable to those normally applicable, or expected to be applicable, in real growth environments for early detection of fungal diseases.

Fungal pathogens and inoculum preparation. Virulent isolates of soil-borne fungal pathogens *R. solani* (RhS) AG-4, *S. rolfsii* (ScR), and *S. sclerotiorum* (ScS) used in this study were obtained from the collection of fungi maintained on potato dextrose agar (PDA, Difco Laboratories, Detroit, Mich.) slants at 20 °C at the Research Centre for Vegetable and Ornamental Crops, Council for Agricultural Research and Economics (CREA), located in Pontecagnano Faiano, Italy. They were previously tested for pathogenicity on wild rocket; stock cultures were stored on PDA slants at 4 °C until use. For each pathogen, the artificial inoculum was prepared by infecting with 20 mycelia plugs (0.5 cm diameter) 500 g millet, previously autoclaved (22 min., 121 °C) and saturated (v/v) with 0.1 × potato dextrose broth (PDB, Difco Laboratories, Detroit, Mich.). After 21 days of incubation in the dark at 25 °C, the infected millet was ready for use after air-drying.

Experiment description. In both experiments, wild rocket (*D. tenuifolia*) cv. Tricia (Enza Zaden, Italy) was sown in black plastic pots (140 mm diameter) filled with autoclaved peat substrate (Klasmann-Deilmann GmbH, Geeste, Germany), at a density of 5 plants pot⁻¹, and grown in a nursery glasshouse to obtain 1-month-old plants. Then, plants were transferred to benches in a climatic chamber at 25 ± 2 °C with a 12-h photoperiod (Exp_Gui) or in an experimental greenhouse (Exp_App). Daily irrigation with dechlorinated sterile water was performed to maintain water holding capacity around 80% of nominal, while a basal NPK mix liquid fertilization was applied twice a week.

For both Exp_Gui and Exp_App, three disease conditions (RhS-D, ScR-D, and ScS-D, disease) were imposed, each at three different levels of disease severity plus a healthy not-inoculated treatment. Each treatment consisted of a total of 10 pots (replicates) for each combination. The different levels of disease severity were obtained by

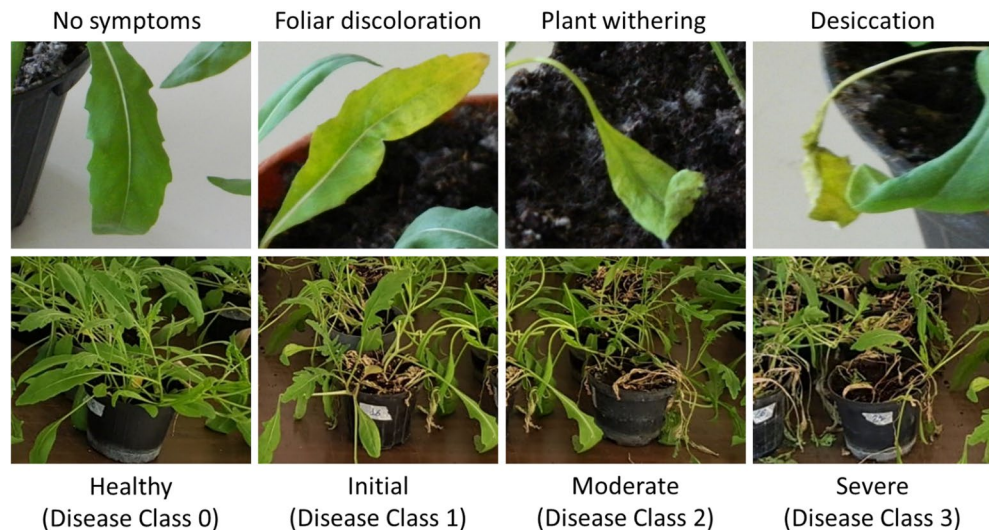


Figure 1. Representative photographs of the four disease classes (0–3) at foliar and pot level.

inoculating different groups of plants at 10, 7, and 3 days before sampling, i.e., spectral acquisitions. Pots were inoculated by incorporating 1 g (dry weight) pot^{-1} of infected millet in the first layer (5 cm depth) of the substrate. Eventually, each pathosystem consisted of 40 pots (200 plants), characterized by different levels of disease severity for a total of 120 pots (600 plants) in the whole trial.

Leaves from Exp_Gui were visually assessed for their disease severity with a score on a 0–3 scale. For pots from Exp_App a visual inspection was also assessed by using a 0–3 rating scale according to the mean symptoms of foliage disease, for each pathosystem. Leaves/pots were classified as: healthy (Disease class 0), and diseased at early (Disease class 1), moderate (Disease class 2), and severe (Disease class 3) degree, according to Manganiello et al.²⁴. Disease class 0 was observed only from the not inoculated healthy controls (Fig. 1).

Reflectance measurements. In Exp_Gui, leaf reflectance (350–2500 nm) was measured by contact under laboratory conditions with a portable non-imaging spectroradiometer (FieldSpec[®] 4 Hi-Res, ASD Inc., Boulder, CO, USA) using an optical fiber contact probe (ASD Plant Probe; ASD Inc., USA) with a 10 mm field of view and an integrated halogen reflector lamp, which minimized atmospheric interference on the recorded signal (active sensor). To increase the quality and homogeneity of the acquired data, the instrument was warmed up for 90 min before measurement. The pre-calibrated Spectral 99% white reference panel was used for calibration, run every 5 min during data acquisition. Each sample scan represented an average of 20 reflectance spectra. Leaves were randomly selected from pots/plants characterized by different disease levels, resulting in a homogenous sampling across disease severity classes. A total of 216, 212, and 222 reflectance acquisitions were obtained for RhS-D, ScR-D and ScS-D, respectively. Leaves were removed from the plants and spectral reflectance was measured immediately on-site on their adaxial side.

For Exp_App, the canopy reflectance was assessed outdoors under full sunlight conditions using the ASD FieldSpec[®] 4 Hi-Res (ASD Inc., Boulder, CO, USA). All spectra were obtained using the spectroradiometer with a 25° field of view (FOV). Potted plants were placed in a fixed plate on a black background, maintaining a vertical distance between the sensor and the top of the plants of 10 cm (passive sensor). Three measurements *per pot* were conducted to obtain an average spectrum in the “canopy dataset” ($n = 40$ for each disease).

Dry weight, leaf area index. Plants in Exp_App were also evaluated for dry weight (DW, g pot^{-1}), leaf area (LA, $\text{cm}^2 \text{pot}^{-1}$), and dry matter content (DM, %) of aerial biomass. Plants were sampled and transferred to the laboratory for aerial fresh and DW determinations, after drying them in an oven at 70 °C until constant weight. Prior to drying, LA was recorded using LI-3100 area meter (Li-Cor Corporation, Lincoln, NE, USA).

Data preparation and analysis. After removing the noisy bands at the extreme wavelengths, the spectral range from 400 to 2450 nm (2051 wavelengths) was analysed. For both leaf and canopy reflectance data, pre-processing involved splice correction to remove the abrupt changes in the recorded values of the neighbouring wavelengths, which appear at the spectral intervals between the three integrated sensors of ASD FieldSpec spectroradiometer. Splice correction was achieved using the commercial software package ASD-View Spec Pro (ASD Inc., Boulder, CO, USA).

Leaf reflectance was assessed under constant light and temperature conditions, so further pre-processing to smooth the spectrum and reduce signal noise was not performed³². Prior to spectral statistical analyses, leaf reflectance was pre-processed using first derivative and mean-centering, in order to reduce the baseline offset by amplifying small spectral features³³. Data pre-treatments was performed with the ParLeS software³⁴. For each disease, data were then randomly divided into two datasets by splitting the observations (approximately 70:30)

into training (calibration) and test (validation) datasets (training set, $n = 150, 149,$ and 160 for RhS-D, ScR-D and ScS-D, respectively; testing set, $n = 66, 63,$ and 62 for RhS-D, ScR-D and ScS-D, respectively).

The RF supervised machine learning algorithm³⁵, a classification algorithm consisting of an ensemble of decision trees, was used by applying R Caret package³⁶ to select the most predictive bands to be used in the construction of the VIs as well as to evaluate the VIs performance in discriminating among the four classes for each disease. To this purpose, a two-step strategy was applied using two types of continuous variables, i.e., (i) reflectance features and (ii) VIs derived from Exp_Gui, to classify the categorical variables (Disease Classes 0, 1, 2, 3) through a set of decision tree process to develop the RF predictive models. The complexity of the input variables was then reduced gradually by selecting at each step the features (bands or VIs) with the highest predictive power through the VSURF R package³⁷ and testing the performance of the restricted variable sets using the Confusion Matrix (R Caret package) and Kappa coefficient. In total, 4 RF models were obtained using: for the first step, (1) all the wavelengths (All λ) and (2) only the selected wavelengths (Selected λ); for the second step, (3) all the derived VIs (All VIs) and (4) only the selected VIs (Selected VIs).

The VIs related to disease severity classes were calculated from the selected wavelengths in the most important regions of the full spectrum. For RhS-D, ScR-D and ScS-D, wavelength selection was performed during the first RF step.

Two band combinations of the spectral indices, Normalized Difference Spectral Indices (NVI) and Simple Ratio Indices (SRs) were generated for all the possible combinations of the selected wavelengths following the equations:

$$NVI_{i-j} = \frac{\text{reflectance}(\text{wavelength}_i) - \text{reflectance}(\text{wavelength}_j)}{\text{reflectance}(\text{wavelength}_i) + \text{reflectance}(\text{wavelength}_j)}$$

$$SR_{i-j} = \frac{\text{reflectance}(\text{wavelength}_i)}{\text{reflectance}(\text{wavelength}_j)}$$

where $\text{reflectance}(\text{wavelength}_i)$ and $\text{reflectance}(\text{wavelength}_j)$ are the spectral reflectance values of two random wavelengths (λ_i and λ_j , respectively).

The newly obtained NVIs and SRs were correlated (Spearman rank correlation)³⁸ with the disease severity levels for each pathogen, to identify the most suitable indicators associated with the identification and development of the pathogenesis.

Finally, newly developed VIs strongly correlated with treatments were tested using the canopy dataset, obtained by canopy reflectance measurements from Exp_App. For each disease, Spearman rank correlations were applied with R software³⁹ to assess the correlation between the VIs and disease severity (at the pot scale) as well as between the VIs and LA, DW and DM, all performed at the pot scale. NVIs and SRs were calculated from the raw spectra after splice correction, as previously indicated. One-way ANOVA followed by the post hoc Least Significant Difference test (LSD) was applied to assess statistical relationships among VIs values over the disease classes using the R package agricolae⁴⁰.

Machine learning modelling, correlations and ANOVA were performed using the statistical software R version 4.0.2³⁹.

Ethics approval. The experimental research and field studies on plants, including the collection of plant material, complied with relevant institutional, national, and international guidelines and legislation.

Results

Disease index and plant growth. All plants in the infected pots developed disease symptoms, as expected, with varying severity depending on the specific pathogen and timing of inoculation. ScR proved to be the most aggressive pathogen producing the basal hydropic lesions immediately after the first day of interaction. Overall, all diseases progressed from hydropic halos/lesions on the plant collar and basal parts of the petioles to rot, wilt, and death of the plant. ScR formed the typical mycelial felt on the targeted basal organs and at a late stage produced the typical light brown spherical sclerotia. On the other hand, ScS signalled its presence with a slight production of white mould, whereas RhS did not burst.

Based on Exp_App, the effects of soil-borne pathogens on plant growth were monitored. Fungal diseases significantly affected plant DW, LA and DM, as they progressed through the four severity levels (Fig. 2).

Hyperspectral fingerprints. Typical reflectance signatures of diseased leaves of wild rocket inoculated with RhS, ScR, and ScS are shown in Fig. 3A–C, respectively. Regardless of the fungal pathogen, the reflectance of leaves of infected plants tended to increase abruptly in the VIS region with advancing disease severity. At the highest disease severity level, the profile of the spectral signature was also affected, especially between 550 and 700 nm, resulting in the altered redshift characteristics and red-edge positions. Despite differences among the pathogens, the reflectance of the most infected leaves decreased in the NIR regions and increased again from around 1400 nm, without affecting the signature patterns (Fig. 3).

Selection of the features by Random Forest modelling. In order to select the most discriminant wavelengths for each pathogen, the RF supervised machine learning algorithm was trained and validated using, respectively, 70 and 30% of the input observations from Exp_Gui. The predictive performance of the models (All λ) is highlighted in each related Caret's Confusion Matrix and related statistics shown in Table 1. RF ran

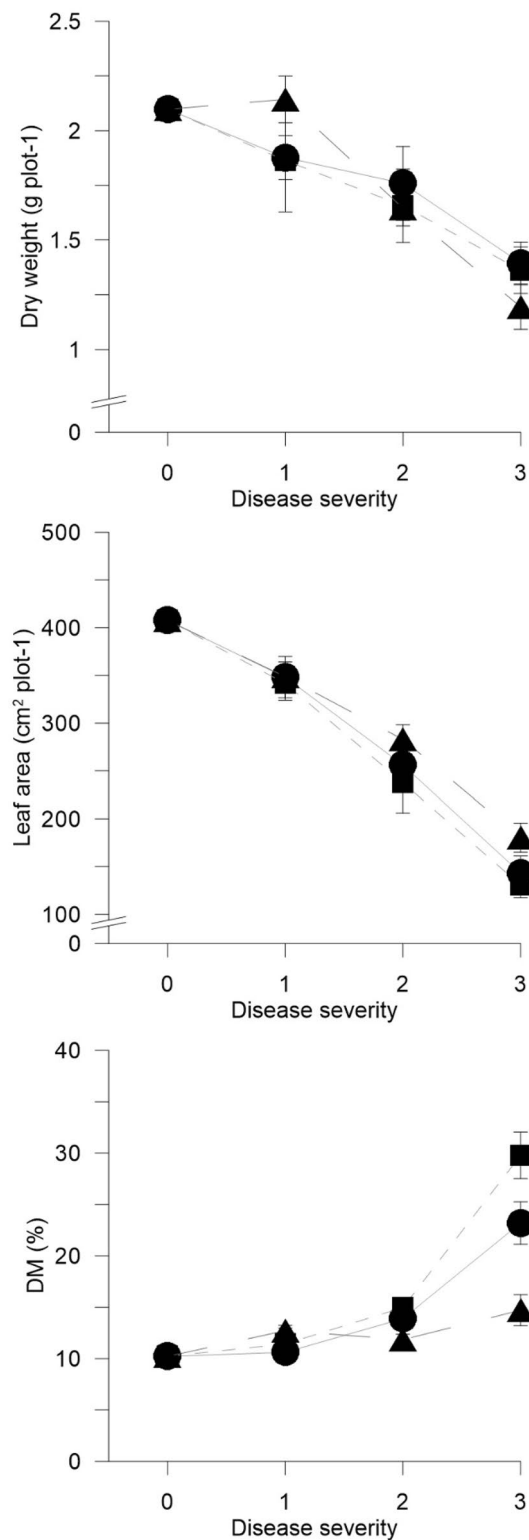


Figure 2. Dry weight (DW, g plot⁻¹), leaf area (LA, cm² plot⁻¹), and dry matter (DM, %) as recorded for wild rocket inoculated with *Rhizoctonia solani* (RhS-D, black circle), *Sclerotium rolfsii* (ScR-D, black square), and *Sclerotinia sclerotiorum* (ScS-D, black triangle), at four disease severity levels (Disease classes 0, 1, 2 and 3 – x-axis) (Exp_App). Data are averages \pm standard errors.

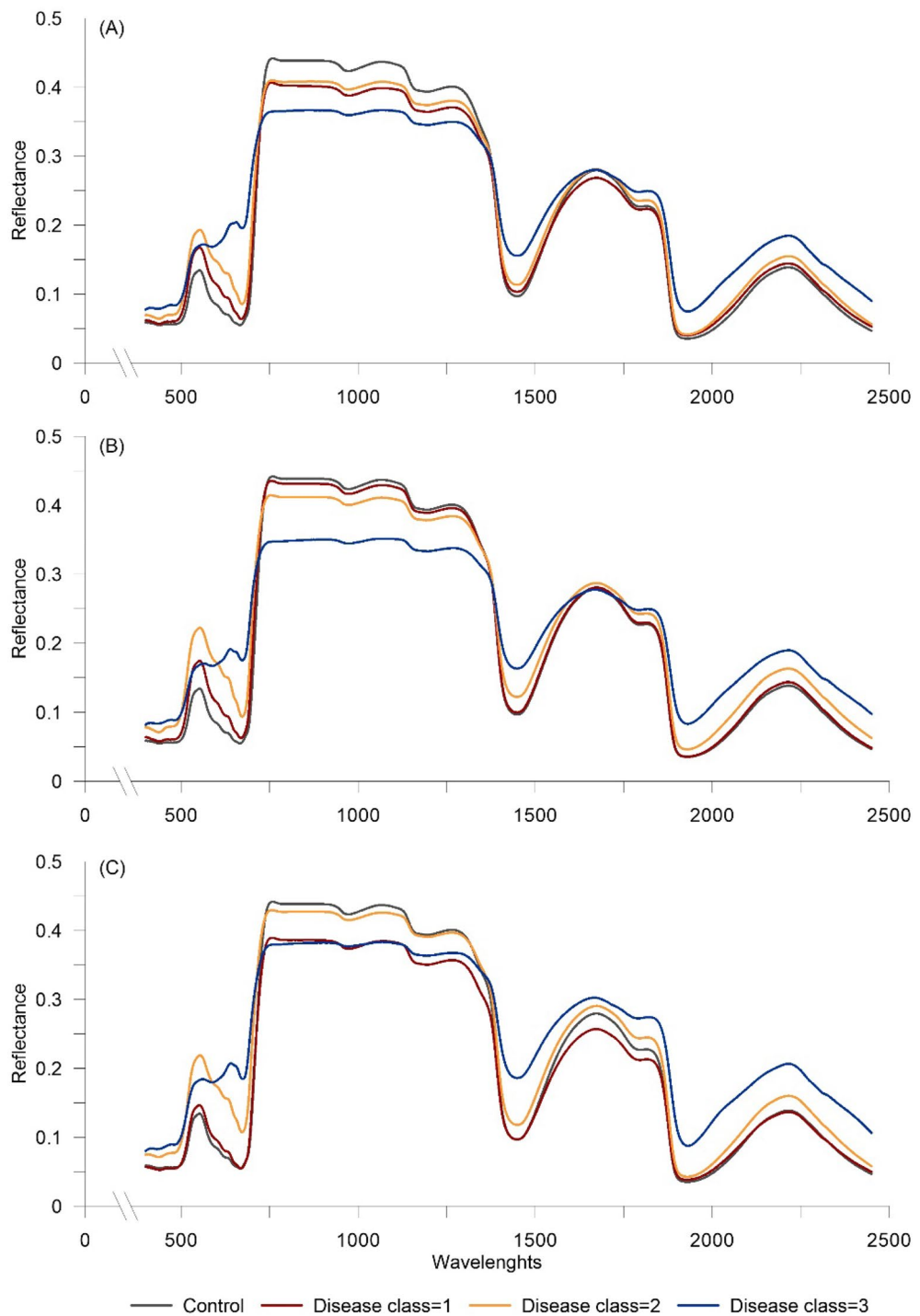


Figure 3. Spectral reflectance as recorded, in the range 350–2500 nm, on wild rocket leaves inoculated with (A) *Rhizoctonia solani* (RhS-D), (B) *Sclerotium rolfsii* (ScR-D), and (C) *Sclerotinia sclerotiorum* (ScS-D) at four disease severity levels (Disease classes 0, 1, 2 and 3) (Exp_Gui).

efficiently on the first derivative reflectance data showing a stable prediction of disease levels compared to the healthy Control, already at the early stages of infection. The higher accuracy level was recorded for ScR-D (0.726) followed by RhS-D and ScS-D (0.625, and 0.500, respectively); these accuracy levels were significantly greater than the no information rate (p -value [$A > N$] < 0.05).

The R package VSURF was then implemented on the obtained RF models in order to remove irrelevant information by the recursive elimination of the smallest important wavelengths and so leading to a subset of explanatory variables highly related to the model response, by minimizing the prediction error. This variable selection method returns a smaller subset of variables focusing more closely on the RF prediction objective avoiding redundancy. The second RF model (Selected λ) was then constructed for each pathogen. In this case, we

		RhS-D				ScR-D				ScS-D						
		True classes				True classes				True classes						
All λ	Predicted classes	0	1	2	3	0	1	2	3	0	1	2	3			
		0	12	9	3	0	0	16	4	2	0	0	14	9	4	1
		1	2	10	8	0	1	2	11	5	0	1	2	3	1	1
		2	0	1	4	1	2	0	2	8	0	2	1	6	6	4
		3	0	0	0	14	3	0	1	1	10	3	0	2	2	10
Accuracy		0.625								0.726						
95% confidence interval		(0.4951, 0.7430)								(0.5977, 0.8315)						
No information rate		0.3125								0.2903						
p -value [A > N]		$2.621 e^{-07}$								$1.725 e^{-12}$						
Kappa		0.4980								0.6294						
Selected λ	Predicted classes	0	1	2	3	0	1	2	3	0	1	2	3			
		0	19	7	1	1	0	17	6	3	0	0	15	9	4	2
		1	1	11	2	0	1	1	9	5	0	1	1	4	1	0
		2	0	1	10	1	2	0	3	7	2	2	1	6	7	4
		3	0	0	1	9	3	0	0	1	8	3	0	1	1	10
Accuracy		0.762								0.661						
95% confidence interval		(0.6379, 0.8602)								(0.5299, 0.7767)						
No information rate		0.3016								0.2903						
p -value [A > N]		$6.623 e^{-14}$								$1.633 e^{-09}$						
Kappa		0.6755								0.5390						
Accuracy										0.500						
95% confidence interval										(0.3743, 0.6257)						
No information rate										0.303						
p -value [A > N]										$6.313 e^{-04}$						
Kappa										0.3390						
Accuracy		0.762								0.661						
95% confidence interval		(0.6379, 0.8602)								(0.5299, 0.7767)						
No information rate		0.3016								0.2903						
p -value [A > N]		$6.623 e^{-14}$								$1.633 e^{-09}$						
Kappa		0.6755								0.5390						

Table 1. Confusion Matrices and overall statistics of Random Forest models trained and validated on (1) all wavebands (All λ) and on (2) the selected wavebands (Selected λ)—reflectance data recorded from wild rocket leaves inoculated with *Rhizoctonia solani* (RhS-D), *Sclerotium rolfsii* (ScR-D), and *Sclerotinia sclerotiorum* (ScS-D) at four disease severities (Disease classes 0, 1, 2 and 3) (Exp_Gui). Wavelengths were selected by the recursive elimination of the smallest important ones to obtain a subset of explanatory variables highly related to the model response.

Disease	VIS-NIR	SWIR
RhS-D	559-602-643-664-671-703-719-724	1377
ScR-D	447-560-567-579-602-636-658-662-663-667-684-724-733-735-854	1958
ScS-D	560-575-601-656-667-719-721-725-726	1135-1905-1908

Table 2. Wavelengths (nm) selected from reflectance data recorded on wild rocket leaves inoculated with *Rhizoctonia solani* (RhS-D), *Sclerotium rolfsii* (ScR-D), and *Sclerotinia sclerotiorum* (ScS-D) (Exp_Gui). The wavelengths were selected starting from RF models by the recursive elimination of the smallest important ones. VIS-NIR = visible-near infrared regions; SWIR = short-wave infrared region.

observed high levels of the proportion of correctly classified cases as well as good metrics, indicating substantial invariance in the predictive value of the models compared to the previous benchmark and so demonstrating the efficiency of band selection (Table 1). In particular, an increase of accuracies of RF models for RhS-D and ScS-D (0.762 and 0.546, respectively), and a decrease for the ScR-D ones, were observed. Moreover, the Balanced Accuracy predicted better the two extreme disease classes (Class 0 and 3)—with values > 0.75—than the intermediate ones (Class 1 and 2), both when all wavelengths were used as entry variables of models and when the RF models were constructed using only the selected wavelengths (Tables S1, S2, S3). This also emerges from the confusion matrices where the misclassified observations tend to zero as we move away from the diagonal (Table 1).

For each telluric pathogenic disease, the selected wavelengths from RF models, most related to the classification response, are reported in Table 2. These bands fell in three regions of the full spectrum, mainly in the VIS-NIR and very few in the SWIR. A total of 9, 16, and 12 wavelengths for RhS-D, ScR-D, and ScS-D, respectively, were selected and combined to build 135, 72, 99 both SRs and NVIs, respectively, for each disease (data not shown). It is worth noting that, regardless of the pathogen, the models selected neighbouring wavelengths in the spectrum (e.g., 559/560 nm; 601/602 nm; around 665 nm; around 724 nm). Some differences were observed for ScR-D in the VIS (i.e., 447 and 854 nm) and, in general among diseases, in the SWIR region.

The so obtained VIs were used for the construction of the third RF classification model (All VIs) for each disease. Indeed, thanks to the flexibility of the RF algorithm, all VIs can be used to get a more accurate prediction of the RhS-D, ScR-D and ScS-D levels. The related confusion matrix showed general accuracy predictions of all VIs based RF models that stood at 0.656, 0.645, and 0.530 for RhS-D, ScR-D, and ScS-D, respectively (Table 3).

		RhS-D				ScR-D				ScS-D						
		True classes				True classes				True classes						
All VIs	Predicted classes	0	1	2	3	0	1	2	3	0	1	2	3			
		0	13	12	2	0	0	15	8	3	0	0	13	8	3	1
		1	1	7	2	1	1	3	8	4	0	1	4	5	2	1
		2	0	1	9	1	2	0	2	7	0	2	0	5	8	5
		3	0	0	2	13	3	0	0	2	10	3	0	2	0	9
Accuracy		0.656								0.645						
95% confidence interval		(0.5270, 0.7705)								(0.5134, 0.7626)						
No information rate		0.3125								0.2903						
<i>p</i> -value [A > N]		1.664 e ⁻⁰⁸								7.577 e ⁻⁰⁹						
Kappa		0.5470								0.5201						
Selected VIs	Predicted classes	0	1	2	3	0	1	2	3	0	1	2	3			
		0	10	8	2	0	0	14	6	1	0	0	14	8	3	1
		1	3	7	5	1	1	4	9	6	0	1	3	5	2	0
		2	1	5	5	3	2	0	3	7	2	2	0	5	7	4
		3	0	0	3	11	3	0	0	2	8	3	0	1	1	11
Accuracy		0.516								0.613						
95% confidence interval		(0.3873, 0.6425)								(0.4807, 0.7340)						
No information rate		0.3125								0.2903						
<i>p</i> -value [A > N]		5.709 e ⁻⁰⁴								1.332 e ⁻⁰⁷						
Kappa		0.3550								0.4746						

Table 3. Confusion Matrices and overall statistics of Random Forest models trained and validated on (3) all the VIs generated by the combinations of the selected wavelengths (All VIs) and on (4) the selected VIs (selected VIs)—reflectance data recorded from wild rocket leaves inoculated with *Rhizoctonia solani* (RhS-D), *Sclerotium rolfsii* (ScR-D), and *Sclerotinia sclerotiorum* (ScS-D) at four disease severities (Disease class 0, 1, 2 and 3) (Exp_Gui). VIs were selected by the recursive elimination of the less important indices to obtain a subset of explanatory variables highly related to the model response.

These models were propaedeutic for the most effective classifier VIs selection; indeed, the subsequent VSURF step allowed the selection of the 12, 10, and 10 most suitable indices, listed in Table 4 and described in the next section, to model disease severity for their ability to classify via RF algorithm the RhS-D, ScR-D and ScS-D. To confirm their consistency for the mentioned objective, the newly obtained VIs fed the fourth RF model (Selected VIs), giving metrics shown in Table 3 as well as in Tables S1, S2, and S3.

Performances of VIs at both leaf and canopy scales. For each pathogen, the selected NVIs and SRs derived from Exp-Gui data are reported in Fig. 4. The highest number of new VIs was found for RhS-D, with 9 wavelengths falling within the ranges of green (559 nm), orange (602 nm), red (643, 664, 671, 703, 719, 724 nm) and SWIR (1377 nm) regions. Ten VIs (7 NVIs and 3 SRs) were obtained to discriminate ScR-D, based on 7 wavelengths of the VIS-NIR ranges, i.e., blue (447 nm), green (560 and 567 nm), yellow (579 nm), orange (602 nm), and red (636, and 733 nm). Lastly, 10 VIs were selected for ScS-D foliar symptoms discrimination: such VIs were developed starting from 8 wavelengths falling within green (560 nm), yellow (575 nm), orange (601 nm), red (656, 667, and 726 nm), and SWIR (1135 and 1908 nm) regions (Table 4). Some VIs were significantly different for all stages of pathogenesis (i.e., for RhS-D: NVI₅₅₉₋₆₀₂, NVI₇₀₃₋₇₂₄, NVI₇₂₄₋₆₀₂, NVI₇₂₄₋₇₁₉, SR₅₅₉₋₆₀₂, SR₇₀₃₋₇₂₄, and SR₁₃₇₇₋₆₆₄; for ScR-D: NVI₅₆₀₋₅₆₇, NVI₅₆₀₋₅₇₉, NVI₅₇₉₋₅₆₇, NVI₆₃₆₋₇₃₃, SR₅₆₀₋₅₇₉, and SR₆₃₆₋₇₃₃), while others discriminated only the highest level of disease severity (i.e., for RhS-D: SR₆₄₃₋₅₅₉; for ScS-D: SR₅₇₅₋₅₆₀ and SR₆₀₁₋₅₆₀) (Fig. 4).

Table 4 also displays the correlations among the selected VIs and the disease severity levels (Spearman correlation coefficient > 0.6 with *p*-value < 0.05). In general, high correlation coefficients were observed for RhS-D and ScR-D (except for NVI₅₅₉₋₆₇₁ for RhS-D and NVI₅₆₀₋₄₄₇ and NVI₅₇₉₋₄₄₇ for ScR-D), while only 4 VIs showed high correlations (> 0.75) with the classes of severity in the case of ScS-D (i.e., NVI₆₀₁₋₁₉₀₈, SR₅₇₅₋₅₆₀, SR₆₀₁₋₅₆₀, and SR₆₅₆₋₇₂₆). However, to evaluate the transferability of the selected VIs to high-throughput environments (i.e., canopy experiments), only the VIs showing Spearman correlation coefficients > 0.60 were considered.

The applicability of those VIs was tested using the canopy dataset from Exp_App. For each pathogen, VIs were calculated starting from canopy reflectance data at the pot scale (Fig. 5). Water absorption bands and noisy spectral regions over 1351–1409 nm and 1801–1949 nm were excluded from the canopy spectral signature and so the NVI₆₀₁₋₁₉₀₈ (ScS-D) was not calculated.

The identified VIs showed a significant relationship (based on Spearman correlation coefficients) with the disease classes of severity (Table 5). RhS-D maintained 11 VIs showing high correlation coefficients with disease levels (ranging from 0.60 to 0.65) but characterized by a good correlation (Pearson coefficient) with some important parameters of crop growth (i.e., LA and DM) (Table 5). The best results were achieved by the NVIs and SRs

Index	Formula	Reference pathogen	Spearman's rank correlation coefficient
NVI ₅₅₉₋₆₀₂	$(R_{559}-R_{602})/(R_{559}+R_{602})$	RhS	-0.788**
NVI ₅₅₉₋₆₇₁	$(R_{559}-R_{671})/(R_{559}+R_{671})$	RhS	-0.382**
NVI ₆₀₂₋₅₅₉	$(R_{602}-R_{559})/(R_{602}+R_{559})$	RhS	0.788**
NVI ₆₄₃₋₅₅₉	$(R_{643}-R_{559})/(R_{643}+R_{559})$	RhS	0.692**
NVI ₇₀₃₋₇₂₄	$(R_{703}-R_{724})/(R_{703}+R_{724})$	RhS	0.741**
NVI ₇₂₄₋₆₀₂	$(R_{724}-R_{602})/(R_{724}+R_{602})$	RhS	-0.613**
NVI ₇₂₄₋₇₁₉	$(R_{724}-R_{719})/(R_{724}+R_{719})$	RhS	-0.718**
NVI ₅₆₀₋₄₄₇	$(R_{560}-R_{447})/(R_{560}+R_{447})$	ScR	0.100
NVI ₅₆₀₋₅₆₇	$(R_{560}-R_{567})/(R_{560}+R_{567})$	ScR	-0.855**
NVI ₅₆₀₋₅₇₉	$(R_{560}-R_{579})/(R_{560}+R_{579})$	ScR	-0.840**
NVI ₅₆₀₋₆₀₂	$(R_{560}-R_{602})/(R_{560}+R_{602})$	ScR	-0.802**
NVI ₅₇₉₋₄₄₇	$(R_{579}-R_{447})/(R_{579}+R_{447})$	ScR	0.337**
NVI ₅₇₉₋₅₆₇	$(R_{579}-R_{567})/(R_{579}+R_{567})$	ScR	0.815**
NVI ₆₃₆₋₇₃₃	$(R_{636}-R_{733})/(R_{636}+R_{733})$	ScR	0.836**
NVI ₅₆₀₋₁₉₀₈	$(R_{560}-R_{1908})/(R_{560}+R_{1908})$	ScS	-0.172*
NVI ₅₇₅₋₁₉₀₈	$(R_{575}-R_{1908})/(R_{575}+R_{1908})$	ScS	-0.081
NVI ₆₀₁₋₁₉₀₈	$(R_{601}-R_{1908})/(R_{601}+R_{1908})$	ScS	0.790**
NVI ₆₅₆₋₆₆₇	$(R_{656}-R_{667})/(R_{656}+R_{667})$	ScS	0.367**
NVI ₆₆₇₋₆₀₁	$(R_{667}-R_{601})/(R_{667}+R_{601})$	ScS	0.182**
SR ₅₅₉₋₆₀₂	R_{559}/R_{602}	RhS	-0.788**
SR ₆₀₂₋₅₅₉	R_{602}/R_{559}	RhS	0.789**
SR ₆₄₃₋₅₅₉	R_{643}/R_{559}	RhS	0.692**
SR ₇₀₃₋₇₂₄	R_{703}/R_{724}	RhS	0.741**
SR ₁₃₇₇₋₆₆₄	R_{1377}/R_{664}	RhS	-0.683**
SR ₅₆₀₋₅₇₉	R_{560}/R_{579}	ScR	-0.840**
SR ₅₇₉₋₅₆₀	R_{579}/R_{560}	ScR	0.840**
SR ₆₃₆₋₇₃₃	R_{636}/R_{733}	ScR	0.836**
SR _{560/1135}	R_{560}/R_{1135}	ScS	0.515**
SR ₅₇₅₋₅₆₀	R_{575}/R_{560}	ScS	0.826**
SR ₆₀₁₋₅₆₀	R_{601}/R_{560}	ScS	0.790**
SR ₆₅₆₋₆₆₇	R_{656}/R_{667}	ScS	0.366**
SR ₆₅₆₋₇₂₆	R_{656}/R_{726}	ScS	0.794**

Table 4. Hyperspectral vegetation normalized difference (NVI) simple ratio (SR) indices (dimensionless) used in this study for wild rocket disease detection. Spearman correlation coefficients between disease severities (Disease classes 0, 1, 2, 3) and the newly developed vegetation indices calculated from reflectance data recorded on rocket leaves inoculated with *Rhizoctonia solani* (RhS), *Sclerotium rolfsii* (ScR), and *Sclerotinia sclerotiorum* (ScS) (Exp_Gui). * $p > 0.05$; ** $p < 0.01$.

reporting the reflectance value at 559 and 602 nm. ScR-D presented the better performing indices among all the investigated pathogens. Those VIs were able to discriminate infection and well related to all measured growth parameters, including the plant DW at harvest. Finally, for ScS-D it was possible to maintain only three indices, characterized by a low correlation with disease severity, LA, and DM (Table 5).

Discussion

Greenhouse cultivation of leafy vegetables such as wild rocket on large areas requires continuous disease monitoring for the ready identification of the spatial/temporal distribution of disease symptoms within the crop, which allows increasing effectiveness (less quantities) and targeting (more precision) of preventive and/or curative control means. For this purpose, proximal detection methods using optoelectronic probes have proved suitable to feed farmers' decision-making processes by ensuring automatic, rapid, non-destructive, and large-scale disease assessment, and reducing the reaction time to the early outbreak²².

In this study, a high-resolution hyperspectral array [i.e., VIS/infrared (IR) spectroscopy] was used to attempt to follow the progression of *R. solani*, *S. rolfsii*, and *S. sclerotiorum* disease symptoms on *D. tenuifolia* through four different severity levels. To the best of our knowledge, this is the first study that investigates the responses of wild rocket to soil-borne fungal pathogens in terms of spectral reflectance. Starting from the full spectral signature we introduced and calculated new vegetation indices aimed at reducing the dimensionality of the dataset, suitable to discriminate between healthy and infected classes of wild rocket leaves, which could be effectively transferable to real (or real like) growing conditions, in order to accelerate disease detection. The methodological information obtained in the present study can be transferred to other (leaf) crop—(soil-borne) pathogen systems.

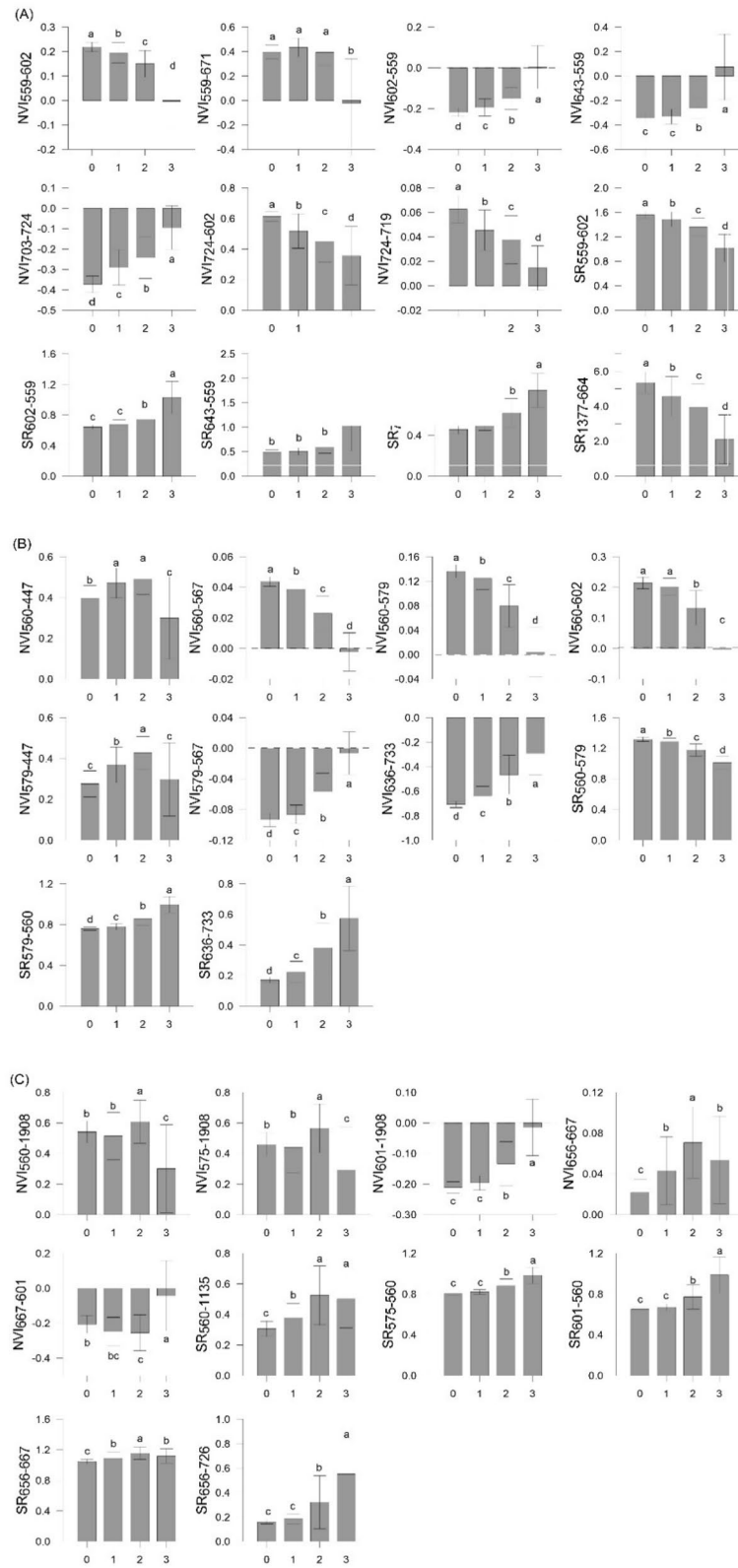


Figure 4. Average of the selected vegetation indices (VIs, dimensionless) calculated from the leaf-reflectance data of wild rocket inoculated with (A) *Rhizoctonia solani* (RhS-D), (B) *Sclerotium rolfsii* (ScR-D), and (C) *Sclerotinia sclerotiorum* (ScS-D) at four disease severity levels (Disease classes 0, 1, 2 and 3) (Exp_Gui). NVI = normalized differences index; SR = simple ratio. Bars with different lowercase letters are significantly different (p -value ≤ 0.05).

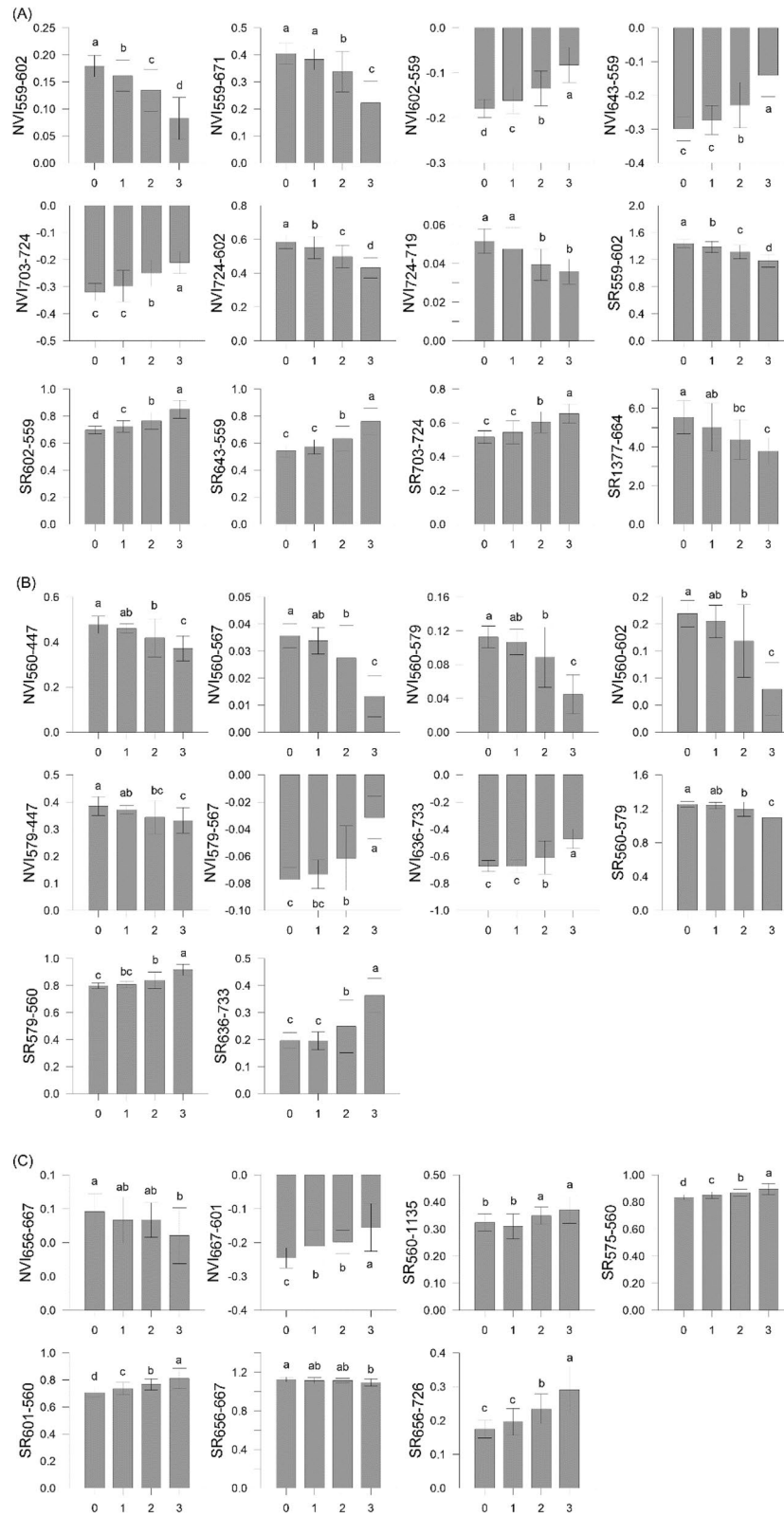


Figure 5. Average of the selected vegetation indices (VIs, dimensionless) calculated from the canopy reflectance data of wild rocket inoculated with (A) *Rhizoctonia solani* (RhS-D), (B) *Sclerotium rolfsii* (ScR-D), and (C) *Sclerotinia sclerotiorum* (ScS-D) at four disease severity levels (Disease classes 0, 1, 2 and 3) (Exp_App). NVI = normalized differences index; SR = simple ratio. Bars with different lowercase letters are significantly different (p -value ≤ 0.05).

Pathogen	Index	DI	DW	LA	DM
RhS-D	NVI ₅₅₉₋₆₀₂	- 0.650*	0.407*	0.756*	- 0.760*
	NVI ₆₀₂₋₅₅₉	0.650*	- 0.407*	- 0.756*	0.760*
	NVI ₆₄₃₋₅₅₉	0.627*	- 0.364*	- 0.743*	0.780*
	NVI ₇₀₃₋₇₂₄	0.629*	- 0.502*	- 0.738*	0.563*
	NVI ₇₂₄₋₆₀₂	- 0.625*	0.500*	0.745*	- 0.609*
	NVI ₇₂₄₋₇₁₉	- 0.604*	0.514*	0.669*	- 0.432*
	SR ₅₅₉₋₆₀₂	- 0.650*	0.408*	0.752*	- 0.732*
	SR ₆₀₂₋₅₅₉	0.650*	0.406*	- 0.756*	0.779*
	SR ₆₄₃₋₅₅₉	0.650*	0.365*	- 0.743*	0.807*
	SR ₇₀₃₋₇₂₄	0.627*	0.503*	- 0.748*	0.589*
	SR ₁₃₇₇₋₆₆₄	- 0.629*	0.406*	0.585*	- 0.412*
ScR-D	NVI ₅₆₀₋₅₆₇	- 0.746*	0.654*	0.862*	- 0.799*
	NVI ₅₆₀₋₅₇₉	- 0.748*	0.672*	0.868*	- 0.801*
	NVI ₅₆₀₋₆₀₂	- 0.764*	0.675*	0.872*	- 0.815*
	NVI ₅₇₉₋₅₆₇	0.748*	- 0.676*	- 0.865*	0.795*
	NVI ₆₃₆₋₇₃₃	0.710*	- 0.674 _{ns}	- 0.844*	0.760*
	SR ₅₆₀₋₅₇₉	- 0.748*	0.668*	0.866*	- 0.791*
	SR ₅₇₉₋₅₆₀	0.748*	- 0.675*	- 0.869*	0.808*
	SR ₆₃₆₋₇₃₃	0.710*	- 0.676*	- 0.841*	0.771*
ScS-D	SR ₅₇₅₋₅₆₀	0.590*	- 0.411*	- 0.625*	0.450*
	SR ₆₀₁₋₅₆₀	0.613*	- 0.404*	- 0.634*	0.494*
	SR ₆₅₆₋₇₂₆	0.607*	- 0.487*	- 0.659*	0.405*

Table 5. Spearman correlation coefficients for disease severities (Disease classes 0, 1, 2, 3) and Pearson correlation coefficients for dry weight (DW, g plot⁻¹), leaf area (LA, cm² plot⁻¹), and dry matter (DM, %) and the newly developed vegetation indices (normalized difference indices: NVI; simple ratios: SR—listed in Table 4) calculated from reflectance data recorded on wild rocket inoculated with *Rhizoctonia solani* (RhS-D), *Sclerotium rolfsii* (ScR-D), and *Sclerotinia sclerotiorum* (ScS-D) (Exp_App). Reflectance data were acquired at canopy scale (named as crop dataset; degrees of freedom = 78), so that was not possible to calculate all the newly developed vegetation indices (see the text for further information). Only indices showing significant Spearman correlation coefficients for DI variable were reported. * $p > 0.05$; *ns* non-significant.

Modelling was performed on an experiment conducted under controlled conditions (i.e., growth chamber) and reflectance data were collected in the laboratory (at leaf scale) using a specific light source⁴¹, thus resulting in high-resolution and high-precision measurements. As expected, fungal diseases influenced the spectral signature: from a qualitative point of view, healthy plants showed low reflectance values in the VIS and SWIR regions as well as high reflectance values in the NIR, highlighting changes in physiological and biological parameters in responses to pathogenesis, i.e., reduction in chlorophyll content, changes in leaf water content, and degeneration of internal leaf structure, respectively^{42–44}. In agreement with previous results⁴¹, a slight blue-shift in the position of the red-edge due to the symptoms of developing necrosis was also observed. However, slight differences among pathogens were detected (e.g., ScR-D near 1700 nm). This deserves further investigation as specific pathosystems are characterized by specific spatiotemporal dynamics, as reported in sugar beet³², tomato⁴⁵, and potato⁴⁶. It is worth specifying that the soil-borne diseases studied generally allow comparable symptomatology, despite differences in terms of disease progression, and their impact on foliage is almost indirect.

The latter aspect might also have been related to the ability of the RF models to discriminate healthy and highly infected leaves with higher accuracy, in comparison with intermediate disease severity, as previously observed in similar studies performed with Propagation Neural Network spectral calibration models on blackleg potato that reduced accuracy on whole plants in field trials²⁵. The RF algorithm represents one of the most common statistical machine learning methods used in modelling and classifying qualitative classes of disease severity from hyperspectral data and has been successfully employed in many host–pathogen combinations^{41,47}. Recently, the RF algorithm has been applied by our group to model the detection of powdery mildew and tracheofusariosis in wild rocket^{48,49}. However, since the continuous narrowband datasets contain redundant spectral information, the selection of significant wavebands was performed, based on the results of RF decision trees⁵⁰.

The main objective of this study was to obtain new spectral VIs, starting from the selected wavelengths in the three full-spectrum regions (i.e., VIS, NIR and SWIR), useful in the scaling up and speeding up of disease detection⁵¹ in wild rocket plants under greenhouse or open-field conditions. In conceptual agreement with the described pipeline, similar hyperspectral data mining was previously conducted to identify the best indices with high healthy/diseased separation capacity of late blight in tomato⁵², *Cercospora* leaf spot in beet⁵³, powdery mildew in squash²⁹, bacterial wilt in peanut²⁷, Yellow Rust in wheat⁵⁴, and *Alternaria* leaf blight in potato⁵⁵.

Regardless of fungal diseases, the new calculated VIs (at leaf scale) were generally effective in separating healthy from infected leaves; however, some VIs could also discriminate intermediate disease intensities. Interestingly, in the case of ScR-D, which seemed to be characterized by the highest hyperspectral spectroscopy

performances, probably due to its greater aggressiveness, the selected NVIs and SRs indices are based on green and light red bands highlighting the effects of disease on leaf pigments concentrations as well as on photosynthetic efficiency⁵⁶. The SR₁₃₇₇₋₆₆₄ was characterized by a good ability to separate disease intensities associated with RhS-D, confirming the role of IR bands to estimate cell damages. In particular, the spectral region centered around 1377 nm represented a key region in the identification of physically damaged mushrooms during the monitoring of their quality⁵⁷. Moreover, for RhS-D, the selected wavelengths in green and orange regions, at 559 and 602 nm, determined high-performance VIs. Those wavelengths have been found ascribed to the leaf chlorophyll content. In particular, λ_{559} , which is normally ignored in most VIs, has been found to be associated with yield and biomass accumulation⁵⁸.

To verify the transferability of de novo VIs, they were tested against the canopy dataset. Close to the spectral regions of the VIs in the present study, MCARI has been previously found to be responsive to the early stage of disease development of *Cercospora* leaf spot and rust on sugar beet³², to tomato chlorophyll content and LAI reduction as affected by bacterial wilting⁵⁹, and to asymptomatic shoot status in presence of abiotic root stress in pepper⁶⁰. On the other hand, the indices estimating pigments, Plant Pigment Ratio and Carotenoid Indices, based respectively on range 550–450 and 500–570 nm, have been, respectively, used to predict plant N status and chlorophyll⁶¹ and carotenoid levels as a proxy of plant stress⁶².

As a matter of fact, the ongoing symptoms associated with soil-borne pathogens, i.e., losses of chlorophyll and other pigments, discoloration, reduced water content, wilting and, finally, desiccation, are closely linked to reduced leaf absorbance in the canopy⁶³. In sugar beet, Reynolds et al.⁶⁴ calculated two narrowband hyperspectral vegetation indices, such as Pigment Specific Simple Ratio (working on chlorophyll a) and modified Spectral Ratio (close to canopy reflectance at 445, 705 and 750 nm), for early detection of *Rhizoctonia* crown and root rot, while chlorophyll/carotenoids dependent SRPI (simple ratio pigment index) was proposed to discriminate the soil borne disease from *Heterodera schachtii* nematode symptoms⁶⁵. Huang and Apan⁶⁶ found VIS–NIR narrow range wavelengths valuable to predict the incidence of *Sclerotinia* rot disease in celery. For most of the literature about VIs, the discrimination between healthy and severely diseased plants leaves is attributable to the strong changes that occurred in the later soil-borne infection stages²⁴. The relevance of these indices seems to be limited to the drastic exclusion of infected plants that can be successfully practised, whereas, in the late stage, disease progression is too advanced to apply preventive strategies.

In the present study, the newly formulated VIs at high-resolution and low-throughput levels (leaf scale) were tested directly on an independent dataset (high-throughput experiment), built on reflectance measurements performed on the canopy, confirming their transferability to ordinary growing and measuring conditions. Interestingly, for all diseases a good correlation between computable VIs and LA was observed.

Conclusions

Our study underlines the importance of scaling up the results of reflectance spectroscopy, performed at leaf scale with a contact probe, under controlled conditions and thus without by environmental factor effects (i.e., light intensity and direction, temperature, and canopy architecture), to larger-scale experiments (canopy scale), characterized by increasingly high-throughput and important for practical applications.

New vegetation indices able to discriminate disease stages were obtained. The most interesting wavelengths fell in the visible and infrared spectral regions, including interesting regions/wavelengths already investigated and previously identified under stress conditions. Extraction of the most significant spectral information from the big dataset is crucial to simplify the production of optoelectronic sensors, suitable for plant disease detection⁴¹ specifically aiming to cheap and innovative surveying devices, to support sustainable disease management in greenhouse or open-field conditions. On perspective, this technology, possibly integrated with different sensors (i.e., thermal sensors and/or 3-D shape sensors)⁶⁷, can improve pathogen detection, since the availability of significant spectral information linked to machine vision-based remote sensing makes feasible the real-time mapping of disease management.

Received: 19 June 2021; Accepted: 14 March 2022

Published online: 24 March 2022

References

- Bennett, R. N., Rosa, E. A. S., Mellon, F. A. & Kroon, P. A. Ontogenic profiling of glucosinolates, flavonoids, and other secondary metabolites in *Eruca sativa* (salad rocket), *Diplotaxis erucoides* (wall rocket), *Diplotaxis tenuifolia* (wild rocket), and *Bunias orientalis* (Turkish rocket). *J. Agric. Food Chem.* **54**, 4005–4015 (2006).
- Jin, J. et al. Analysis of phytochemical composition and chemoprotective capacity of rocket (*Eruca sativa* and *Diplotaxis tenuifolia*) leafy salad following cultivation in different environments. *J. Agric. Food Chem.* **57**, 5227–5234 (2009).
- Pasini, F., Verardo, V., Cerretani, L., Caboni, M. F. & D'Antuono, L. F. Rocket salad (*Diplotaxis* and *Eruca* spp.) sensory analysis and relation with glucosinolate and phenolic content. *J. Sci. Food Agric.* **91**, 2858–2864 (2011).
- Løkke, M. M., Seefeldt, H. F. & Edelenbos, M. Freshness and sensory quality of packaged wild rocket. *Postharvest Biol. Technol.* **73**, 99–106 (2012).
- Freshplaza. Italy rocket exports valued at 30–40 million Euro. www.freshplaza.com/article/2098430/italy-rocket-exports-valued-at-30-40-million-euro/ (Accessed 19 June 2021) (2012).
- Bonasia, A., Conversa, G., Lazzizzera, C. & Elia, A. Post-harvest performance of ready-to-eat wild rocket salad as affected by growing period, soilless cultivation system and genotype. *Postharvest. Biol. Technol.* **156**, 110909 (2019).
- Martínez-Sánchez, A. et al. Baby-leaf and multi-leaf of green and red lettuces are suitable raw materials for the fresh-cut industry. *Postharvest Biol. Technol.* **63**, 1–10 (2012).
- Colelli, G. & Elia, A. Physiological and technological aspects of fresh-cut horticultural products. *Italus Hortus* **16**, 55–78 (2009).
- Elgueta, S., Moyano, S., Sepúlveda, P., Quiroz, C. & Correa, A. Pesticide residues in leafy vegetables and human health risk assessment in North Central agricultural areas of Chile. *Food Addit. Contam.* **10**, 105–112 (2017).

10. Chaudhry, M. M. A. *et al.* Feasibility study for the surface prediction and mapping of phytonutrients in minimally processed rocket leaves (*Diplotaxis tenuifolia*) during storage by hyperspectral imaging. *Comput. Electron. Agric.* **175**, 105575 (2020).
11. Nicoletti, R., Raimo, F. & Miccio, G. *Diplotaxis tenuifolia*: Biology, production and properties. *Eur. J. Plant Sci. Biotechnol.* **1**, 36–43 (2007).
12. Gilardi, G., Garibaldi, A. & Gullino, M. L. Emerging pathogens as a consequence of globalization and climate change: Leafy vegetables as a case study. *Phytopathol. Mediterr.* **57**, 146–152 (2018).
13. Gilardi, G., Gullino, M. L. & Garibaldi, A. Emerging foliar and soil-borne pathogens of leafy vegetable crops: A possible threat to Europe. *EPPO Bull.* **48**, 116–127 (2018).
14. Garibaldi, A., Minuto, A. & Gullino, M. L. First report of Sclerotinia stem rot and watery soft rot caused by *Sclerotinia sclerotiorum* on sand rocket (*Diplotaxis tenuifolia*) in Italy. *Plant Dis.* **89**, 11 (2005).
15. Gullino, M. L., Gilardi, G. & Garibaldi, A. Ready to eat salad crops: A plant pathogen's haven. *Plant Dis.* **103**, 2153–2170 (2019).
16. Garibaldi, A. & Gullino, M. L. Emerging soilborne diseases of horticultural crops and new trends in their management. *Acta Hortic.* **883**, 37–47 (2010).
17. Caruso, G., Parrella, G., Giorgini, M. & Nicoletti, R. Crop systems, quality and protection of *Diplotaxis tenuifolia*. *Agriculture* **8**, 55 (2018).
18. Pane, C. *et al.* Response of rocket salad germplasm (*Eruca* and *Diplotaxis* spp.) to major pathogens causing damping-off, wilting and leaf spot diseases. *Arch. Phytopathol. Plant Protect.* **50**, 167–177 (2017).
19. Pane, C. *et al.* Managing Rhizoctonia damping-off of rocket (*Eruca sativa*) seedlings by drench application of bioactive potato leaf phytochemical extracts. *Biology* **9**, 270 (2020).
20. Zaccardelli, M. *et al.* Stepwise-selected *Bacillus amyloliquefaciens* and *B. subtilis* strains from composted aromatic plant waste able to control soil-borne diseases. *Agriculture* **10**, 30 (2020).
21. Lamichhane, J. R. *et al.* Identifying obstacles and ranking common biological control research priorities for Europe to manage most economically important pests in arable, vegetable and perennial crops. *Pest Manag. Sci.* **73**, 14–21 (2017).
22. Lowe, A., Harrison, N. & French, A. P. Hyperspectral image analysis techniques for the detection and classification of the early onset of plant disease and stress. *Plant Methods* **13**, 80 (2017).
23. Sapate, N. M., Deshmukh, R. R. & Janse, P. V. Spectral discrimination of healthy and diseased plants using non imaging hyperspectral data—A review. *Int. J. Res. Eng. Appl. Manag.* **1922**, 85–89 (2019).
24. Manganiello, G. *et al.* Functional hyperspectral imaging by high-related vegetation indices to track the wide-spectrum Trichoderma biocontrol activity against soil-borne diseases of baby-leaf vegetables. *Front. Plant Sci.* **12**, 630059 (2021).
25. Bienkowski, D., Aitkenhead, M. J., Lees, A. K., Gallagher, C. & Neilson, R. Detection and differentiation between potato (*Solanum tuberosum*) diseases using calibration models trained with non-imaging spectrometry data. *Comput. Electron. Agric.* **167**, 105056 (2019).
26. Karadağ, K., Tenekeci, M. E., Taştaltın, R. & Bilgili, A. Detection of pepper Fusarium disease using machine learning algorithms based on spectral reflectance. *Sustain. Comput.-Inform. Syst.* **28**, 100299 (2020).
27. Chen, T. *et al.* Early detection of bacterial wilt in peanut plants through leaf-level hyperspectral and unmanned aerial vehicle data. *Comput. Electron. Agric.* **177**, 105708 (2020).
28. Junges, A. H., Almança, M. A. K., Fajardo, T. V. M. & Ducati, J. R. Leaf hyperspectral reflectance as a potential tool to detect diseases associated with vineyard decline. *Trop. Plant Pathol.* **45**, 522–533 (2020).
29. Abdulridha, J., Ampatzidis, Y., Roberts, P. & Kakarla, S. C. Detecting powdery mildew disease in squash at different stages using UAV-based hyperspectral imaging and artificial intelligence. *Biosyst. Eng.* **197**, 135–148 (2020).
30. Leoni, C. *et al.* *Sclerotium rolfii* dynamics in soil as affected by crop sequences. *Appl. Soil Ecol.* **75**, 95–105 (2014).
31. Xue, J. & Su B. Significant remote sensing vegetation indices: A review of developments and applications. *J. Sens.* **2017**, 1353691 (2017).
32. Mahlein, A. K., Steiner, U., Dehne, H. W. & Oerke, E. C. Spectral signatures of sugar beet leaves for the detection and differentiation of diseases. *Precis. Agric.* **11**, 413–431 (2010).
33. Fu, X., Chen, J., Fu, F. & Wu, C. Discrimination of talcum powder and benzoyl peroxide in wheat flour by near-infrared hyperspectral imaging. *Biosyst. Eng.* **190**, 120–130 (2020).
34. Rossel, R. A. V. ParLeS: Software for chemometric analysis of spectroscopic data. *Chemom. Intell. Lab. Syst.* **90**, 72–83 (2008).
35. Adam, E., Deng, H., Odindi, J., Abdel-Rahman, E. M. & Mutanga, O. Detecting the early stage of Phaeosphaeria Leaf Spot infestations in maize crop using in situ hyperspectral data and guided regularized Random Forest Algorithm. *J. Spectrosc.* **2017**, 6961387 (2017).
36. Kuhn, M. Building predictive models in R using the caret package. *J. Stat. Softw.* **28**(1), 1–26 (2008).
37. Genuer, R., Poggi, J. M. & Tuleau-Malot, C. VSURF: An R package for variable selection using random forests. *R J.* **7**, 19–33 (2015).
38. Conover, W. J. *Practical Nonparametric Statistics* 3rd edn. (Wiley, 1999).
39. R core team. *The R Foundation for Statistical Computing* (2020).
40. de Mendiburu, F. agricolae: Statistical procedures for agricultural research. R package version 1.3-5. <https://CRAN.R-project.org/package=agricolae> (Accessed 03 Jan 2022) (2021)
41. Zhang, N. *et al.* A review of advanced technologies and development for hyperspectral-based plant disease detection in the past three decades. *Remote Sens.* **12**, 3188 (2020).
42. Omran, E. S. E. Early sensing of peanut leaf spot using spectroscopy and thermal imaging. *Arch. Agron. Soil Sci.* **63**, 883–896 (2017).
43. Skoneczny, H. *et al.* Fire blight disease detection for apple trees: Hyperspectral analysis of healthy, infected and dry leaves. *Remote Sens.* **12**, 2101 (2020).
44. Su, W. H. Advanced machine learning in point spectroscopy, RGB-and hyperspectral-imaging for automatic discriminations of crops and weeds: A review. *Smart Cities* **3**, 767–792 (2020).
45. Lu, J., Ehsani, R., Shi, Y., de Castro, A. I. & Wang, S. Detection of multi-tomato leaf diseases (late blight, target and bacterial spots) in different stages by using a spectral-based sensor. *Sci. Rep.* **8**, 1–11 (2018).
46. Gold, K. M. *et al.* Hyperspectral measurements enable pre-symptomatic detection and differentiation of contrasting physiological effects of late blight and early blight in potato. *Remote Sens.* **12**, 286 (2020).
47. Pourazar, H., Samadzadegan, F. & Dadrass Javan, F. Aerial multispectral imagery for plant disease detection: Radiometric calibration necessity assessment. *Eur. J. Rem. Sens.* **52**, 17–31 (2019).
48. Pane, C., Manganiello, G., Nicastro, N., Cardi, T. & Carotenuto, F. Powdery mildew caused by *Erysiphe cruciferarum* on wild rocket (*Diplotaxis tenuifolia*): Hyperspectral imaging and machine learning modeling for non-destructive disease detection. *Agriculture* **11**, 337 (2021).
49. Pane, C., Manganiello, G., Nicastro, N. & Carotenuto, F. Early detection of wild rocket tracheofusariosis using hyperspectral image-based machine learning. *Remote Sens.* **14**, 84 (2022).
50. Conrad, A. O. *et al.* Machine learning-based presymptomatic detection of Rice Sheath Blight using spectral profiles. *Plant Phenomics* **2020**, 8954085:1–10 (2020).
51. Al-Saddik, H., Simon, J. C. & Cointault, F. Development of spectral disease indices for 'Flavescence Dorée' grapevine disease identification. *Sensors* **17**, 2772. <https://doi.org/10.3390/s17122772> (2017).
52. Zhang, M., Qin, Z., Liu, X. & Ustin, S. L. Detection of stress in tomatoes induced by late blight disease in California, USA, using hyperspectral remote sensing. *Int. J. Appl. Earth Obs. Geoinf.* **4**, 295–310 (2003).

53. Bergsträsser, S. *et al.* HyperART: Non-invasive quantification of leaf traits using hyperspectral absorption-reflectance transmittance imaging. *Plant Methods* **11**, 1 (2015).
54. Guo, A. *et al.* Wheat yellow rust detection using UAV-based hyperspectral technology. *Remote Sens.* **13**, 123 (2021).
55. Van De Vijvera, R. *et al.* In-field detection of *Alternaria solani* in potato crops using hyperspectral imaging. *Comput. Electron. Agric.* **168**, 105106 (2020).
56. Nguyen, H. T. & Lee, B. W. Assessment of rice leaf growth and nitrogen status by hyperspectral canopy reflectance and partial least square regression. *Eur. J. Agron.* **24**, 349–356 (2006).
57. Esquerre, C., Gowen, A. A., Downey, G. & O'Donnell, C. P. Wavelength selection for development of a near infrared imaging system for early detection of bruise damage in mushrooms (*Agaricus bisporus*). *J. Near Infrared Spectrosc.* **20**, 537–546 (2012).
58. Mhango, J. K., Harris, W. E. & Monaghan, J. M. Relationships between the spatio-temporal variation in reflectance data from the Sentinel-2 satellite and potato (*Solanum tuberosum* L.) yield and stem density. *Remote Sens.* **13**, 4371 (2021).
59. Srivastava, A. *et al.* Detection of bacterial wilt disease (*Pseudomonas solanacearum*) in Brinjal using hyperspectral remote sensing. *Int. Arch. Photogramm. Remote Sens. Spat. Inf. Sci.* **XLII-3/W6**, 515–520 (2019).
60. Weksler, S. *et al.* Pepper plants leaf spectral reflectance changes as a result of root rot damage. *Remote Sens.* **13**, 980 (2021).
61. Wang, Z. J. *et al.* Prediction of grain protein content in winter wheat (*Triticum aestivum* L.) using plant pigment ratio (PPR). *Field Crops Res.* **90**, 311–321 (2004).
62. Zarco-Tejada, P. J. *et al.* Previsual symptoms of *Xylella fastidiosa* infection revealed in spectral plant-trait alterations. *Nat. Plants* **4**, 432–439 (2018).
63. Thenkabail, P. S. & Lyon, J. G. Hyperspectral remote sensing of vegetation and agricultural crops. *Photogramm. Eng. Remote Sens.* **80**, 697–723 (2014).
64. Reynolds, G. J., Windels, C. E., MacRae, I. V. & Laguette, S. Remote sensing for assessing Rhizoctonia crown and root rot severity in sugar beet. *Plant Dis.* **96**, 497–505 (2012).
65. Hillnhütter, C., Mahlein, A. K., Sikora, R. A. & Oerke, E. C. Remote sensing to detect plant stress induced by *Heterodera schachtii* and *Rhizoctonia solani* in sugar beet fields. *Field Crops Res.* **122**, 70–77 (2011).
66. Huang, J. F. & Apan, A. Detection of Sclerotinia rot disease on celery using hyperspectral data and partial least squares regression. *J. Spat. Sci.* **51**, 129–142 (2006).
67. Traversari, S. *et al.* Precision agriculture digital technologies for sustainable fungal disease management of ornamental plants. *Sustainability* **13**, 3707 (2021).

Acknowledgements

Authors would like to thank Maria Assunta Dattoli for help with plant measurements.

Author contributions

A.G. and C.Pa. designed the research and interpreted data. A.G., A.P., C.Pl., and C.Pa. done the experiments and acquired data. A.G., N.N., and C.Pa. done the data analysis. A.G., T.C., and C.Pa. have drafted, reviewed, and edited the original manuscript. All authors have read and agreed to the published version of the manuscript.

Funding

This study was funded by the Italian Ministry of Agriculture, Food and Forestry Policies (MiPAAF), through the AgriDigit programme—sub-project ‘Tecnologie digitali integrate per il rafforzamento sostenibile di produzioni e trasformazioni agroalimentari (AgroFiliera)’ (DM 36503.7305.2018 of 20/12/2018).

Competing interests

The authors declare no competing interests.

Additional information

Supplementary Information The online version contains supplementary material available at <https://doi.org/10.1038/s41598-022-08969-5>.

Correspondence and requests for materials should be addressed to C.P.

Reprints and permissions information is available at www.nature.com/reprints.

Publisher's note Springer Nature remains neutral with regard to jurisdictional claims in published maps and institutional affiliations.



Open Access This article is licensed under a Creative Commons Attribution 4.0 International License, which permits use, sharing, adaptation, distribution and reproduction in any medium or format, as long as you give appropriate credit to the original author(s) and the source, provide a link to the Creative Commons licence, and indicate if changes were made. The images or other third party material in this article are included in the article's Creative Commons licence, unless indicated otherwise in a credit line to the material. If material is not included in the article's Creative Commons licence and your intended use is not permitted by statutory regulation or exceeds the permitted use, you will need to obtain permission directly from the copyright holder. To view a copy of this licence, visit <http://creativecommons.org/licenses/by/4.0/>.

© The Author(s) 2022